Research Square

Preprints are preliminary reports that have not undergone peer review.
They should not be considered conclusive, used to inform clinical practice,
or referenced by the media as validated information.

Deep-Subwavelength Plasmon Polariton Atomic Cavity Nano-detector for Polarimetric Terahertz Detection and Imaging

Huanjun Chen

chenhj8@mail.sysu.edu.cn

State Key Lab of Optoelectronic Materials and Technologies, Guangdong Province Key Lab of Display Material and Technology, School of Electronics and Information Technology, Sun Yat-sen University

https://orcid.org/0000-0003-4699-009X

Shaojing Liu

State Key Lab of Optoelectronic Materials and Technologies, Guangdong Province Key Lab of Display Material and Technology, School of Electronics and Information Technology, Sun Yat-sen University

Hongjia Zhu

State Key Lab of Optoelectronic Materials and Technologies, Guangdong Province Key Lab of Display Material and Technology, School of Electronics and Information Technology, Sun Yat-sen University

Ningsheng Xu

Guangdong Province Key Laboratory of Display Material and Technology, School of Electronics and Information Technology, Sun Yat-sen University

Ximiao Wang

Guangdong Province Key Laboratory of Display Material and Technology, Sun Yat-sen University

Runli Li

State Key Lab of Optoelectronic Materials and Technologies, Guangdong Province Key Lab of Display Material and Technology, School of Electronics and Information Technology, Sun Yat-sen University

Hai Ou

State Key Lab of Optoelectronic Materials and Technologies, Guangdong Province Key Lab of Display Material and Technology, School of Electronics and Information Technology, Sun Yat-sen University

Shangdong Li

Sun Yat-sen University

Yanlin Ke

State Key Lab of Optoelectronic Materials and Technologies, Guangdong Province Key Lab of Display Material and Technology, School of Electronics and Information Technology, Sun Yat-sen University

Runze Zhan

State Key Lab of Optoelectronic Materials and Technologies, Guangdong Province Key Lab of Display Material and Technology, School of Electronics and Information Technology, Sun Yat-sen University

Shaozhi Deng
State Key Lab of Optoelectronic Materials and Technologies, Guangdong Province Key Lab of Display Material and Technology, School of Electronics and Information Technology, Sun Yat-sen University
https://orcid.org/0000-0003-1830-2026

Article

Keywords:

Posted Date: October 21st, 2026

DOI: https://doi.org/10.21203/rs.3.rs-11273694/v1

License: This work is licensed under a Creative Commons Attribution 4.0 International License.
Read Full License

Additional Declarations: There is no conflict of interest

Deep-Subwavelength Plasmon Polariton Atomic Cavity Nano-detector for Polarimetric Terahertz Detection and Imaging

Shaojing Liu[†], Hongjia Zhu[†], Ningsheng Xu, Ximiao Wang, Runli Li, Hai Ou, Shangdong Li, Yanlin Ke, Runze Zhan, Huanjun Chen[*], and Shaozhi Deng[*]

State Key Laboratory of Optoelectronic Materials and Technologies, Guangdong Province Key Laboratory of Display Material and Technology, School of Electronics and Information Technology, Sun Yat-sen University, Guangzhou 510275, China

*Corresponding author. E-mail: chenhj8@mail.sysu.edu.cn; stsdsz@mail.sysu.edu.cn

[†]These authors contributed equally to this work.

Abstract

Room-temperature, miniaturized, multiparameter terahertz (THz) detectors with ultrafast response, particularly in the high-frequency THz regime (> 0.3 THz), are essential for next-generation information perception, including radar imaging, remote sensing, semiconductor inspection, and scalable THz focal-plane arrays. Yet, deep-subwavelength miniaturization ($<\lambda_0/50$) remains challenging because the reduced interaction volume between long-wavelength THz waves and nanoscale absorbers leads to intrinsically weak light–matter coupling. Here, we present a graphene plasmon polariton atomic cavity (PPAC) nano-detector that overcomes this limitation by exploiting resonant THz field confinement in graphene PPACs, enabling efficient light–matter interaction within an ultracompact channel. The architecture integrates graphene PPAC arrays with asymmetric metal contacts, where graphene simultaneously serves as the THz absorber and charge transport channel. Channel shortening accelerates the photothermoelectric response by reducing the hot-carrier diffusion length, capacitance, and contact parasitics. Leveraging plasmon resonances and optimized carrier dynamics, the detector achieves broadband (0.53–4.24 THz), polarization- and frequency-sensitive THz detection with a polarization ratio of 93, responsivity of 1007 V/W, noise-equivalent power of 16 pW/Hz$^{0.5}$, detectivity of 2.9×10^7 Jones, and a 230 ps response. This deep-subwavelength device represents the smallest and fastest multifunctional detector reported to date in the high-frequency THz regime and enables, for the first time, polarization-resolved shielded imaging that distinguishes conductive from non-conductive features within encapsulated chips, advancing compact, high-speed, room-temperature THz technologies.

Introduction

Terahertz (THz) radiation (0.1–10 THz) provides rich spectral, polarization, and phase information beyond conventional intensity imaging, enabling characterization of structural and electronic anisotropies at micro- and nanoscale dimensions[1–4]. In particular, high-frequency THz operation (> 0.3 THz), where wavelengths approach the characteristic dimensions of microelectronic features, is critical for improving spatial resolution and enabling shielded imaging of concealed conductive structures in integrated circuits and semiconductor chips. Realizing such capabilities requires miniaturized detectors that simultaneously provide room-temperature operation, ultrafast response, and intrinsic polarimetric functionality, enabling polarization- and frequency-resolved THz detection for high-resolution imaging[5–7].

However, existing THz detectors remain poorly suited for this regime. Thermal detectors, including Golay cells, thermopiles, and bolometers, provide room-temperature operation but are limited by slow thermal response[8]. Electronic detectors such as high-electron-mobility transistors and Schottky barrier diodes offer fast response and high sensitivity, yet their bandwidth decreases significantly in the high-frequency THz regime[9]. Photonic detectors based on narrow-bandgap semiconductors can achieve high sensitivity but often require cryogenic cooling[10]. Moreover, polarization-resolved THz detection typically relies on external polarizers, wave plates, or metasurfaces, which introduce optical complexity and hinder monolithic integration[11]. Therefore, a detector architecture that simultaneously enables efficient electromagnetic field coupling, intrinsic polarization sensitivity, fast detection, and deep-subwavelength miniaturization remains highly desirable[12,13].

Van der Waals (vdW) two-dimensional (2D) materials, particularly graphene, provide a promising platform for THz micro- and nano-detectors owing to their atomic thickness, tunable electronic properties, and high carrier mobility at room temperature[14]. Accordingly, THz detectors based on graphene and other 2D materials have been widely developed[15–20], particularly through the excitation of optical resonances[21]. Nevertheless, deep-subwavelength scaling remains challenging because the reduced interaction volume between long-wavelength THz radiation and atomically thin materials leads to inefficient light–matter coupling. In addition, weak intrinsic THz anisotropy in most 2D materials requires integration with external polarization-resolved structures, increasing device complexity and footprint[6,22–24]. Overcoming these limitations requires a strategy that simultaneously enhances THz interaction and sustains intrinsic detector functionalities at nanoscale dimensions. Recently, graphene plasmon polariton atomic cavities (PPACs) have enabled monolithic multiparameter THz detection by exploiting resonant enhancement in patterned graphene nanostructures, eliminating bulky

antennas and external polarization optics[5]. However, conventional PPAC geometries still impose a trade-off between resonance frequency, device size, and detection performance, limiting further miniaturization.

Here, we demonstrate that engineering the aspect ratio of rectangular graphene PPACs enables resonance-preserving device scaling, providing a route toward deep-subwavelength THz detectors in which resonant field confinement within the PPACs enhances light–matter interaction, while the graphene layer simultaneously serves as the THz absorber and charge-transport channel. The detector employs an asymmetric graphene channel comprising rectangular PPACs and unpatterned graphene, contacted by dissimilar metal electrodes. In contrast to circular PPACs, whose resonance is mainly determined by diameter[5], the rectangular PPAC geometry introduces an additional degree of freedom through the aspect ratio, enabling channel shortening and lateral scaling while preserving the target plasmonic resonance frequency. This anisotropic geometry further provides frequency- and polarization-resolved absorption through dipolar excitation along the long axis of the PPACs. Meanwhile, reducing the channel dimensions accelerates the photothermoelectric (PTE) response by shortening hot-carrier diffusion paths and lowering capacitance and contact parasitics. As a result, we realize an atomically thin detector with a lateral channel area of only 2 μm × 16 μm (~λ_0/60), achieving broadband (0.53–4.24 THz), frequency- and polarization-resolved detection with a polarization ratio of 93, responsivity of 1007 V/W (98 V/W), and noise-equivalent power (NEP) of 16 pW/Hz$^{0.5}$ (165 pW/Hz$^{0.5}$), referenced to absorbed (incident) THz power. The detector exhibits an experimentally measured response time of 230 ps, with simulations projecting a response time of ~60 ps for the 2 μm-channel device, establishing it, to our knowledge, as the smallest and fastest multifunctional detector reported to date in the high-frequency THz regime (see Supplementary Table S1). This detector enables, for the first time, polarization-resolved shielded imaging of encapsulated semiconductor chips that distinguishes conductive from non-conductive regions, establishing a pathway toward compact, high-speed, multifunctional THz imaging systems.

Results

Geometry-controlled plasmon polariton resonances in rectangular graphene PPACs

Deep-subwavelength THz detection requires a resonant element that can preserve light–matter interaction even when the photoactive region is much smaller than the free-space wavelength[25]. We therefore first examined how the geometry of rectangular graphene PPACs controls the resonance frequency, absorption strength, and polarization selectivity. Finite-

difference time-domain (FDTD) simulations were performed for normally incident THz waves, with the polarization angle $\theta = 0°$ defined as the electric field parallel to the long axis of the PPACs (Fig. 1a).

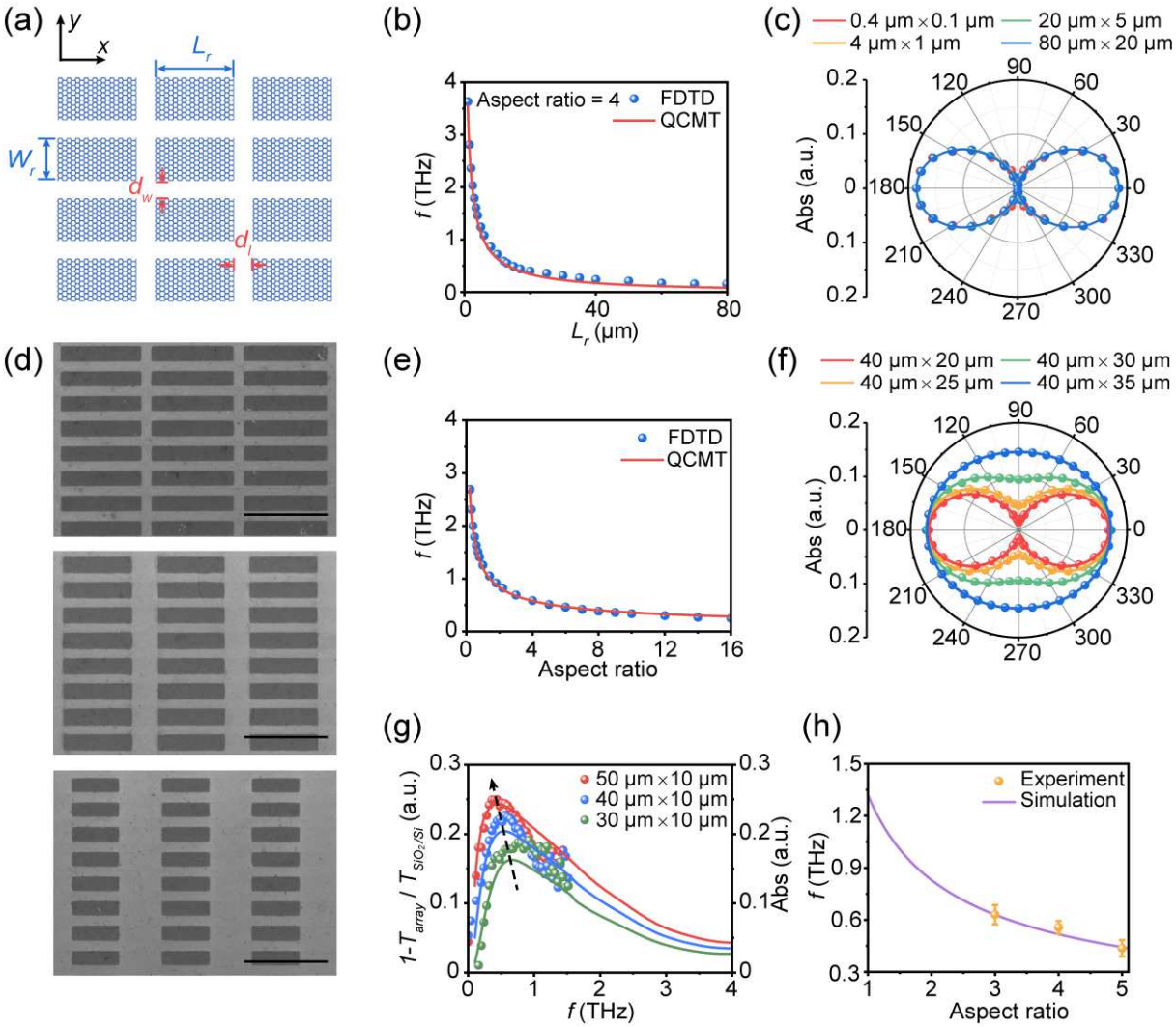

Fig. 1 Geometry-controlled THz plasmon polariton resonances in rectangular graphene PPACs. a, Schematic of the graphene rectangular PPAC array. L_r and W_r denote the resonator length and width, and d_w and d_l denote the inter-resonator spacings along the x and y directions, respectively. **b**, Simulated resonance frequency f as a function of L_r for a fixed aspect ratio of 4 ($L_r = 4W_r$). **c**, Simulated polarization dependence of the resonance absorption for PPACs with a fixed aspect ratio of 4; θ is the angle between the THz polarization and the long axis of the PPAC. **d**, SEM images of rectangular PPAC arrays with dimensions of 50 μm × 10 μm, 40 μm × 10 μm, and 30 μm × 10 μm. Scale bars: 50 μm. **e**, Simulated f as a function of aspect ratio from 0.2 to 16 for a fixed W_r = 5 μm. **f**, Simulated polarization dependence of resonance absorption for PPACs with aspect ratios from 1.1 to 2. **g**, Experimental (dots) and simulated (lines) THz absorption spectra of the PPAC arrays shown in (**d**). **h**, Experimental (symbols) and simulated (line) resonance frequencies extracted from (**g**) as a function of aspect ratio.

For PPACs with a fixed aspect ratio $AR = L_r/W_r = 4$, the resonance redshifts systematically as L_r increases from 1 to 80 μm (Fig. 1b and Fig. S1a). This trend agrees with the resonance frequencies obtained from quasistatic coupled-mode theory (QCMT; Supplementary Note S1)[26], showing that the resonance can be predictably engineered through cavity geometry. The resonance intensity also changes with L_r because the filling factor of the array varies with resonator size. The polarization response shows a dipole-like behavior: absorption is strongest when the incident electric field is aligned with the long axis and is suppressed when the field is rotated towards the short axis (Fig. 1c). The polarization ratio was defined as,

$$PR = \frac{I_{max}}{I_{min}} \tag{1}$$

where I_{max} and I_{min} are the maximum and minimum absorption intensities at the resonance frequency. For representative PPACs with dimensions of 0.4 μm × 0.1 μm, 4 μm × 1 μm, 20 μm × 5 μm, and 80 μm × 20 μm, the calculated *PR* values are 154, 217, 211, and 127, respectively, showing that strong polarization selectivity is preserved over a wide range of cavity sizes when the aspect ratio is fixed.

The aspect ratio provides an additional degree of freedom that is absent in circular or square PPACs[5]. For a fixed width W_r = 5 μm, increasing L_r redshifts the resonance across the 0.1–4.0 THz range (Figs. 1e and Fig. S1b), while the polarization response remains governed by a dipole-like plasmon mode (Fig. 1f). For rectangular PPACs with L_r = 40 μm and W_r increasing from 20 to 35 μm, *PR* decreases from 11.1 to 1.2, indicating that higher aspect ratios strengthen polarization selectivity. Thus, unlike high-symmetry geometries such as squares, circles, or regular hexagons, rectangular PPACs provide resonance-frequency tunability and polarization discrimination within a single planar graphene geometry, without increasing the device footprint.

Polarization-resolved simulations further reveal two orthogonal cavity modes (Fig. S2). As θ increases from 0° to 90°, the long-axis resonance weakens, while a higher-frequency short-axis resonance emerges. Near-field distributions confirm that this second resonance originates from plasmon excitation along the PPAC width. This dual-resonance behavior allows a simple rectangular graphene cavity to provide both frequency- and polarization-resolved responses without multilayer metamaterials or additional anisotropic optical components. The inter-cavity spacings d_w and d_l also modulate the collective plasmon response (Fig. S3)[5]. Reducing d_l strengthens attractive dipole coupling between adjacent cavities along the polarization direction, lowers the restoring force, and redshifts the resonance. It also increases the resonance

intensity by enhancing near-field coupling and suppressing radiative loss. In contrast, increasing d_w weakens repulsive coupling between neighboring cavities in the transverse direction and likewise reduces the effective restoring force. These trends indicate that both single-cavity aspect ratio and array-level coupling can be used to position the resonance while maintaining strong field confinement.

The simulated trends were verified experimentally by THz time-domain spectroscopy (THz-TDS, BATOP TDS-1008). Rectangular PPAC arrays with unit sizes of 50 μm × 10 μm, 40 μm × 10 μm, and 30 μm × 10 μm were fabricated on monolayer graphene transferred onto high-resistivity SiO_2/Si substrates (Fig. 1d, see Methods). Raman spectra show prominent G and 2D bands at 1580 and 2700 cm^{-1}, respectively, with no obvious D peak and a single-Lorentzian 2D band with a full width at half maximum of 32 cm^{-1}, confirming the high quality of the patterned graphene (Fig. S4a). The absorption was extracted from,

$$Abs = 1 - \frac{T_{\mathrm{PPAC}}}{T_{\mathrm{SiO_2/Si}}} \tag{2}$$

where T_{PPAC} and $T_{\mathrm{SiO_2/Si}}$ are the transmissions of the PPAC array on SiO_2/Si and the bare substrate, respectively. The measured absorption spectra, with incident polarization parallel to the long axis of the PPACs, reproduce the simulated absorption spectra and resonance shifts with aspect ratio (Fig. 1g and 1h), validating rectangular PPACs as tunable THz cavities for resonant field confinement in atomically thin graphene.

Monolithic PPAC detector for ultrafast frequency- and polarization-resolved detection

Having established geometry-controlled plasmonic resonant confinement, we next integrated rectangular PPACs into a monolithic graphene detector. The device consists of an asymmetric graphene channel contacted by source and drain electrodes (Fig. 2a). Here, the graphene channel refers to the photoactive monolayer graphene region between the source and drain electrodes, where THz absorption and subsequent photoelectric conversion occur, as define in Refs. [5], [15], and [16]. One side of the channel contains a rectangular PPAC array connected by graphene nanoribbons, whereas the other side is unpatterned graphene. The representative detector has a total channel area of 20 μm × 16 μm and a channel length L_c = 20 μm (Fig. 2b). Individual PPACs of 2.5 μm × 400 nm produce a pronounced absorption resonance at 2.52 THz (Fig. S4b). Ti/Au electrodes were formed by ultraviolet lithography, metal deposition, and lift-off (see Methods). The linear dark *I–V* curve and a device resistance of 3852 Ω indicate Ohmic contact between graphene and the electrodes (Fig. S4c), which is important for extracting a zero-bias PTE signal.

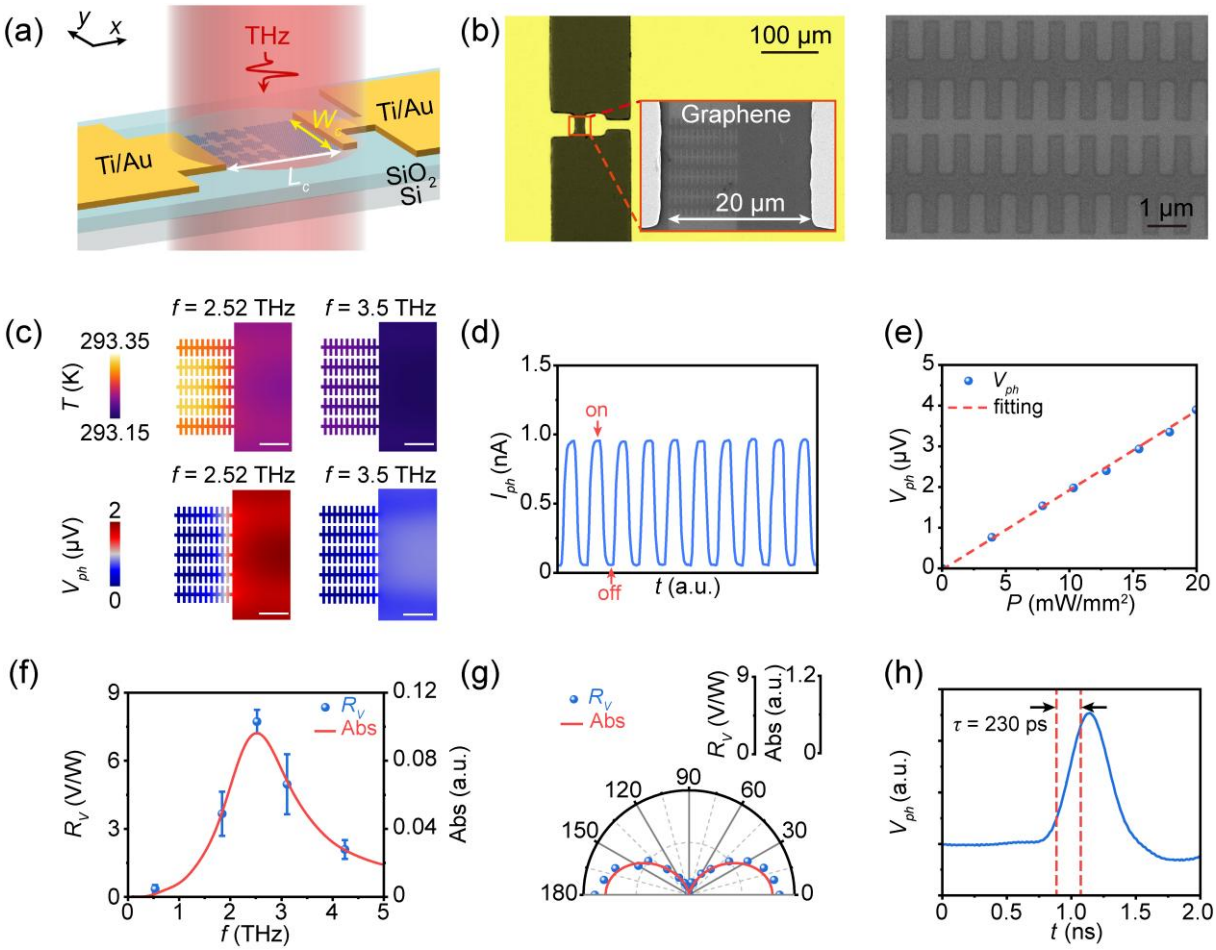

Fig. 2 Monolithic PPAC nano-detector with bias-free, frequency- and polarization-resolved PTE response. a Schematic of the detector, where an asymmetric graphene channel bridges two Ti/Au electrodes. The channel comprises a rectangular PPAC array connected by graphene nanoribbons on one side and unpatterned graphene on the other. **b** Optical image and SEM images of the fabricated detector and PPAC array. **c** Simulated temperature and electric-potential distributions under resonant excitation at 2.52 THz and off-resonant excitation at 3.5 THz. Scale bar: 5 μm. **d** Zero-bias photocurrent under periodically modulated 2.52-THz illumination. **e** Photovoltage as a function of illumination power. **f** Measured frequency-dependent photoresponse (symbols) compared with simulated THz absorption (line). **g** Polarization-dependent photoresponse (symbols) compared with simulated polarization-resolved absorption (line). **h** Time-resolved photovoltage response to a broadband THz pulse (0.1–3.0 THz).

The detection mechanism is governed by the conversion of resonantly generated hot carriers into a PTE photocurrent or photovoltage. Finite-element (FEM) simulations (COMSOL Multiphysics, see Methods) were used to calculate the electromagnetic field, temperature profile, and electric potential under resonant and off-resonant excitation (Fig. 2c and Fig. S5).

At 2.52 THz, the PPAC resonance concentrates the THz field inside the patterned graphene region (Fig. S5, left pannel), increases local absorption, and generates a hot-carrier population. Because the patterned PPAC side and the unpatterned graphene side absorb THz radiation differently, a lateral temperature gradient develops across the channel (Fig. 2c, upper left panel). The resulting zero-bias photovoltage is described by,

$$V_{\mathrm{ph}} = -\int_0^{L_c} S(x)\nabla T(x)dx \tag{3}$$

$$S(x) = -\frac{\pi^2 k_{\mathrm{B}}{}^2 T(x)}{3e}\left(\frac{\mathrm{d}\ln\sigma}{\mathrm{d}E}\right)\Bigg|_{E=E_{\mathrm{f}}} \tag{4}$$

where $S(x)$ is the Seebeck coefficient, $\nabla T(x)$ is the temperature gradient, k_{B} is the Boltzmann constant, $T(x)$ is the local temperature, e is the elementary charge, σ is the graphene conductivity, and E_{f} is the Fermi level. The simulated temperature and potential maps show that the PPAC side becomes hotter than the unpatterned side and that the induced potential drives a spontaneous current without external bias (Fig. 2c, left panels; Fig. S5, right panel). At 3.5 THz, where the PPAC resonance is not excited, the field confinement, temperature gradient, and photovoltage are all strongly reduced (Fig. 2c, right panels). Resonant THz confinement of the PPAC array therefore directly determines the strength and spectral selectivity of the PTE response.

Under 2.52-THz illumination polarized along the long axis of the PPACs, the detector generates reproducible zero-bias photocurrent over repeated on/off cycles (Fig. 2d), and the corresponding photovoltage scales linearly with incident power (Fig. 2e). The voltage responsivity R_{V} is calculated as,

$$R_{\mathrm{V}} = \frac{V_{\mathrm{ph}}}{P_{\mathrm{eff}}} = \frac{I_{\mathrm{ph}} \times R}{P_{\mathrm{eff}}} \tag{5}$$

$$I_{\mathrm{ph}} = \frac{2\pi\sqrt{2}V_{\mathrm{lock}}}{4G} \tag{6}$$

where I_{ph} and V_{ph} are the photocurrent and photovoltage, R is the channel resistance, V_{lock} is the lock-in output voltage, G is the current-preamplifier gain, and P_{eff} is the effective power coupled to the active region. It is worth noting that the spot size of the THz beam (~1 mm diameter) is substantially larger than the active channel area of our antenna-free detectors. This contrasts with most conventional THz detectors integrated with antennas, where the device area is typically comparable to the beam size[15,22,23]. As a result, the incident power is not efficiently concentrated on the active region in our case, highlighting the importance of evaluating

responsivity with respect to the effective power rather than the total incident power. Specifically, two effective-power definitions were used. The absorbed-power definition is[5,16],

$$P_{\text{eff}} = \frac{P_0 \times S_{\text{device}}}{S_0} \times \eta \tag{7}$$

where S_{device} is the graphene-channel area, S_0 and P_0 are the spot area and total THz power, and η is the PPAC absorption at resonance frequency obtained from the simulated absorption spectrum. The second definition omits η and corresponds to the incident power projected onto the active area.

In our study, the PPAC detector uses plasmonic resonances to confine the THz field and localize absorption within the graphene channel. Therefore, the use of absorbed power as a meaningful metric for responsivity evaluation more directly reflects the intrinsic photoelectric conversion efficiency of the PPAC architecture. This metric highlights the role of resonant light–matter interaction in compensating the reduced interaction volume at deeply subwavelength scales. For the L_c = 20 μm detector, R_V is 7 V/W when referenced to absorbed power and 0.7 V/W when referenced to incident power, demonstrating that the PPAC resonance maintains measurable responsivity despite the compact antenna-free active area (Supplementary Table S1).

Noise measurements show 1/f noise below ~1 kHz and Johnson–Nyquist noise at higher frequencies (Fig. S4d). Because the device remains stable up to a modulation frequency of 7.8 kHz (Fig. S4e), the NEP was evaluated using the Johnson-noise limit,

$$\text{NEP} = \frac{\sqrt{4k_B TR}}{R_V} \tag{8}$$

and the specific detectivity D^* was calculated as,

$$D^* = \frac{\sqrt{A}\sqrt{B}}{\text{NEP}} \tag{9}$$

where A is the effective device area and B is the measurement bandwidth. At 2.52 THz, the detector reaches an NEP of 1.2 nW/Hz$^{0.5}$ and $D^* = 2.8 \times 10^5$ Jones when referenced to absorbed power. Device-to-device statistics further show mean values of V_{ph} = 0.9 μV, R_V = 4.8 V/W, NEP = 4.1 nW/Hz$^{0.5}$, and $D^* = 2.6 \times 10^5$ Jones (Fig. S6), with the spread mainly attributed to variations in graphene quality and fabrication uniformity. Further improvements in R_V and D^*, along with NEP reduction, can be achieved by optimizing graphene quality, fabrication processes, and device area, as discussed below.

The same resonance that enhances absorption also gives the detector frequency selectivity. Measurements at 0.53, 1.84, 2.52, 3.11, and 4.24 THz show that the strongest response occurs

at 2.52 THz, matching the simulated absorption maximum (Fig. 2f). Detectors with varied PPAC dimensions exhibit distinct resonance frequencies and corresponding peak responses (Figs. S7 and S8). For example, the 2.5 μm × 400 nm PPAC detector peaks at 2.52 THz, whereas a larger 30 μm × 20 μm PPAC detector peaks near 0.5 THz. The PPAC geometry therefore provides a direct route to frequency-resolved THz detection over a broad spectral range.

The anisotropic cavity resonance also enables intrinsic polarization selectivity. When the incident polarization is rotated with a half-wave plate, the detector responsivity follows an inverted figure-eight pattern that matches the simulated polarization-dependent PPAC absorption (Fig. 2g). The device polarization ratio, PR_{device}, is defined as,

$$PR_{\text{device}} = \frac{V_{\text{phmax}}}{V_{\text{phmin}}} \tag{10}$$

where V_{phmax} and V_{phmin} are the maximum and minimum photovoltages as the incident polarization is rotated. Under 2.52-THz illumination, the detector with L_c = 20 μm achieves PR_{device} = 93, representing one of the highest polarization ratios reported for antenna- and metamaterial-free 2D-material-based THz detectors (Supplementary Table S1). FDTD simulations show that the electrode-induced field response has the opposite polarization dependence to the PPAC absorption (Fig. S9), confirming that the observed inverted figure-eight response originates primarily from the PPAC resonance rather than the metal contacts.

The response time τ is a critical parameter characterizing the performance of the PPAC nano-detector. The PTE mechanism, combined with the short channel of the detector and the high carrier mobility of graphene, enables high-speed detection performance[27]. The temporal response was evaluated using a broadband THz pulse from 0.1 to 3.0 THz (Fig. 2h, see Methods). To obtain a sufficiently large signal for the time-domain measurement, multiple graphene channels were connected in series to form a 3-mm-long device (Fig. S10). The measured photovoltage follows the incident THz pulse and gives a response time of 230 ps, already faster than most reported 2D-material-based THz detectors (Supplementary Table S1). As shown below, this response can be further accelerated by reducing the hot-carrier diffusion path in deep-subwavelength channels[28].

Deep-subwavelength scaling through field confinement and contact engineering

Miniaturization usually weakens THz detector response because shrinking of the active area reduces the interaction volume between THz wave and the detector channel. We therefore investigated whether resonant confinement in PPAC detectors can overcome this scaling trade-off. A series of devices with channel lengths from 50 to 2 μm were fabricated while keeping

the channel width fixed at 16 μm (Fig. S11a). The shortest device has an active area of only 2 μm × 16 μm, corresponding to ~λ_0/60 at 2.52 THz. The measured resistance increases from ~1800 Ω to ~8000 Ω as L_c increases from 2 to 50 μm (Fig. S12), consistent with the longer transport path. Under 2.52-THz illumination, the photovoltage shows two regimes (Fig. 3a). For L_c < 10 μm, it remains nearly constant even as the active channel is aggressively shortened. For $L_c \geq 10$ μm, the photovoltage increases with channel length but at a reduced rate, gradually saturating for L_c > 20 μm. Simulations including both the electrodes and the PPAC array reproduce this trend and clarify the mechanism (see Methods). In an electrode-only configuration, heat accumulation and potential drops remain localized near the metal contacts (Fig. 3f, right panel). When the PPAC array is included, resonant absorption raises the temperature in the graphene cavity region and extends the potential variation into the channel (Fig. 3f, left panel). The difference between the two simulations increases with channel length (Fig. S13a), indicating that the PPAC contribution becomes more important in longer channels. In contrast, for L_c < 10 μm, the isolated PPAC-induced photovoltage is small (Fig. S13b), and the response is dominated by strong field confinement between closely spaced electrodes (Fig. S14).

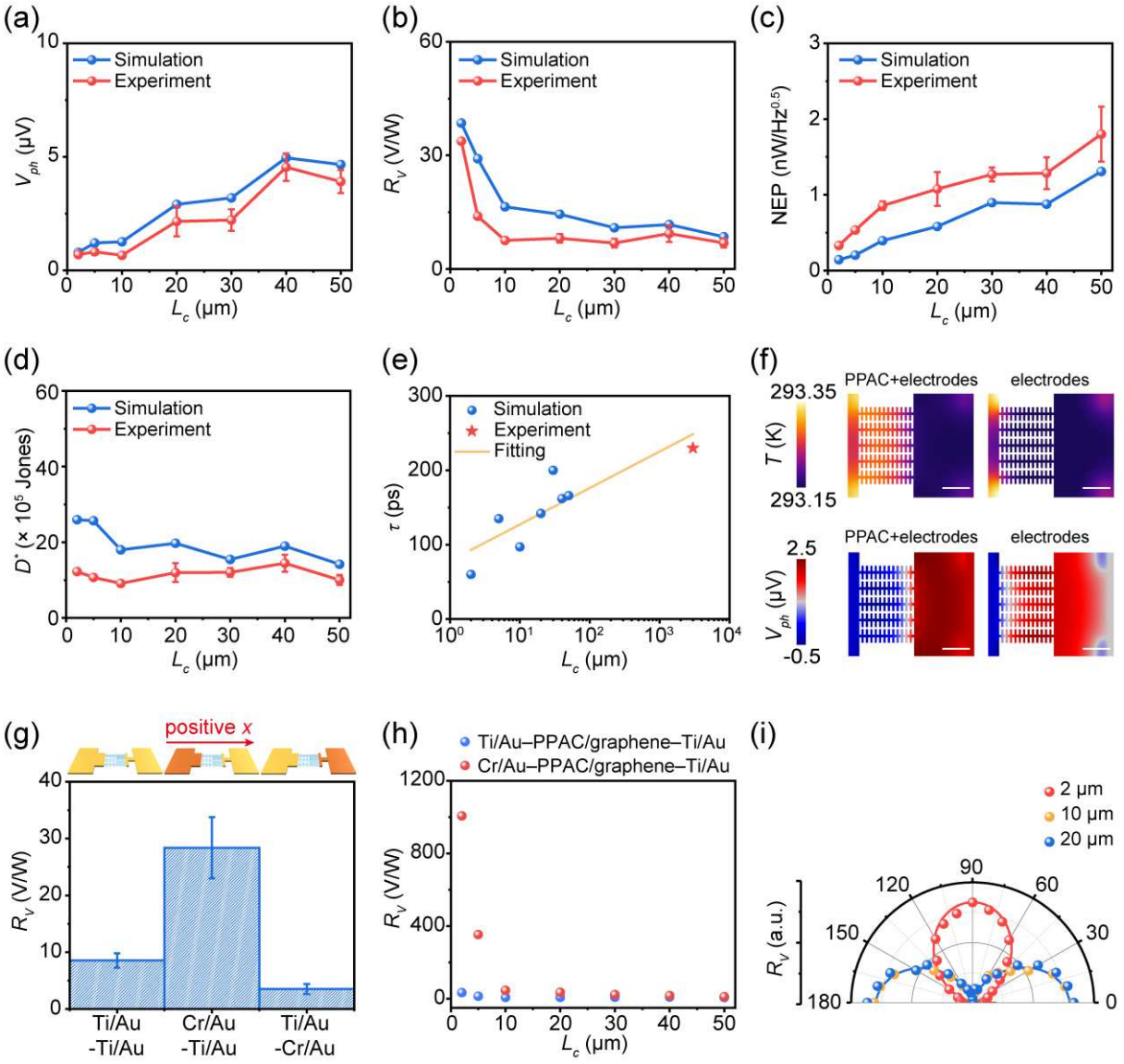

Fig. 3 Deep-subwavelength scaling of graphene PPAC THz detectors. a–d Channel-length dependence of photovoltage, R_V, NEP, and D^*. These R_V, NEP, and D^* values are obtained when reference to absorbed power. Experimental and simulated data are shown by red and blue symbols, respectively. **e** Simulated response time as a function of channel length. The red star denotes the measured response of the 3-mm-long series device, and the orange line shows a linear fit to the simulated trend. **f** Simulated temperature and electric-potential distributions for a 20-μm-channel detector with both electrodes and PPACs included (left) and with electrodes only (right). Scale bar: 5 μm. **g** Responsivity of detectors with Ti/Au–Ti/Au, Cr/Au–Ti/Au, and Ti/Au–Cr/Au contact configurations. The metal electrodes consist of 10 nm Ti or Cr, capped with 100 nm Au (top panel). **h** Channel-length dependence of responsivity for symmetric and asymmetric-contact detectors. **i** Polarization-dependent THz photoresponse for detectors with L_c = 2 (red), 10 (orange), and 20 μm (blue) compared with simulated polarization-resolved absorption.

This dual-regime behavior explains why the photovoltage does not collapse under deep-subwavelength scaling. In short-channel devices, electrode-mediated near-field confinement compensates for the reduced number of PPAC units and the smaller active area. In longer devices, PPAC-mediated resonant absorption and hot-carrier thermal diffusion dominate the PTE voltage. For devices with L_c > 10 μm, when the cumulative length of the PPAC array remains below the thermal diffusion length of 15.9 μm (Supplementary Note S2), adding PPAC units leads to a collective increase in local heating, particularly near the leftmost PPAC–electrode interface. This thermal accumulation enhances the lateral temperature gradient across the device, thereby increasing the thermoelectric photovoltage (Fig. 3f, Fig. S15a, and Supplementary Note S2). In contrast, once the PPAC array exceeds the thermal diffusion length, the incremental contribution from additional PPAC units becomes negligible. These remote units no longer substantially affect the temperature at the electrode interface, resulting in a stabilized temperature gradient and, consequently, a saturated photovoltage output (Fig. S15b, c). Accordingly, the photovoltage increases monotonically with channel length and asymptotically saturates in long-channel devices (L_c > 20 μm). Thus, the response is governed by the balance among field confinement, resonant absorption, and hot-carrier diffusion, rather than by geometric area alone.

The above mechanism converts channel shortening into a performance advantage. When L_c is reduced from 50 to 2 μm, the effective absorbed power decreases by a factor of ~30 because of the smaller active area (Fig. S11b). The photovoltage, however, decreases by only a factor of ~6 and remains nearly unchanged for L_c < 10 μm (Fig. 3a). As a result, R_V increases by a factor of 4.9, while NEP calculated from the current noise power density spectra of the corresponding channel lengths decreases by a factor of 5.5 over the same scaling range (Fig. 3b, c and Fig. S16). Meanwhile, the specific detectivity D^* shows a more modest increase, improving by a factor of 1.2 (Fig. 3d). These improvements become especially pronounced when the channel length falls below 10 μm. At L_c = 2 μm, the symmetric-contact detector reaches R_V = 34 V/W and NEP = 0.3 nW/Hz$^{0.5}$ when referenced to absorbed power within an active area of 32 μm^2. These results show that resonant and contact-mediated THz confinement can compensate the reduced interaction volume that normally limits deep-subwavelength detectors.

Channel scaling also accelerates the PTE response. Because the output of an individual short-channel device is too small for direct time-domain measurement in our current setup, response times were simulated for L_c = 2–50 μm (Fig. 3e and Supplementary Note S3). The

calculated response decreases as the channel is shortened and reaches ~60 ps for L_c = 2 μm, a 2.8-fold reduction relative to the 50-μm device. The measured response of the 3-mm-long series device lies on the extrapolated trend, supporting the validity of the model for shorter channels.

The origin of this speed improvement was assessed by comparing the relevant time scales of PTE detection: hot-carrier thermal diffusion (τ_{diff}), the resistor−capacitor (RC) time constant, and the optical bandwidth of the PPAC resonance. These characteristic quantities are[4,29],

$$\tau_{diff} = \frac{L_D^2 C_{el}}{\kappa} \tag{11}$$

$$f_{RC} = \frac{1}{2\pi RC} \tag{12}$$

$$f_{3dB} = \frac{c}{2nW_c Q} \tag{13}$$

where L_D is the hot-carrier thermal diffusion length, C_{el} is the electronic heat capacity, κ is the thermal conductivity, c is the speed of light, n is the substrate refractive index (1.955 for SiO_2), W_c is the channel width, and Q is the quality factor of the PPAC resonator. Here, $Q = \omega_{res}/\Delta\omega$, with ω_{res} and $\Delta\omega$ denoting the resonance angular frequency and linewidth, respectively. The optical bandwidth is not limiting: using W_c = 16 μm and $Q \approx 1.5$ gives f_{3dB} on the order of 1 THz, corresponding to a sub-picosecond optical time scale. The RC contribution was estimated using the device equivalent resistance and a lumped channel capacitance (Supplementary Note S4), yielding RC-limited frequency f_{RC} of ~35–885 GHz, corresponding to RC-limited response times of ~0.4–10 ps. These values are nearly one to two orders of magnitude shorter than the simulated response times, indicating that RC delay is not the primary speed-limiting process in the miniaturized PPAC devices. Nevertheless, reducing the channel length substantially lowers the capacitance and contact parasitics, thereby suppressing the RC delay that commonly limits larger-area or bulk detector architectures.

The response is instead primarily governed by hot-carrier thermal diffusion. Reducing L_c from 50 to 2 μm decreases the effective diffusion length from ~15.9 μm to below 2 μm (Supplementary Note S2). Using reported room-temperature graphene diffusivities of $D = \kappa/C_{el} \approx 100-5000$ cm^2/s[30], τ_{diff} is estimated to be ~8–505 ps, consistent with the simulated response range of 60–200 ps. This agreement indicates that channel scaling accelerates the PTE response primarily by shortening the hot-carrier diffusion path, while the reduced capacitance and contact parasitics enable efficient readout of the generated photovoltage. This diffusion-limited picture highlights the physical advantage of the PPAC architecture. The plasmonic cavity concentrates THz absorption within a deeply subwavelength graphene channel, preserving efficient PTE conversion even as the active length is reduced. At the same time, the shortened

thermal diffusion path and smaller parasitic capacitance jointly support ultrafast operation, leading to a projected response time of ~60 ps for the 2 μm-channel device. These results show that PPAC scaling not only improves integration density and maintains responsivity, but also provides a physical route to faster room-temperature THz detection.

To further enhance the PTE voltage, we introduced asymmetric metal contacts. Devices with Ti/Au–PPAC/graphene–Ti/Au, Cr/Au–PPAC/graphene–Ti/Au, and Ti/Au–PPAC/graphene–Cr/Au configurations were fabricated with the same 20 μm × 16 μm channel and PPAC dimensions of 400 nm × 2.5 μm, all resonant at 2.52 THz (Fig. S17). Under 2.52-THz illumination, the Cr/Au–PPAC/graphene–Ti/Au device gives the largest responsivity, whereas the reversed Ti/Au–PPAC/graphene–Cr/Au device gives the smallest response (Fig. 3g). This polarity dependence reflects the vector addition of two currents, plasmon polariton resonance (PPR)-induced hot-carrier current I_0 and contact-induced current I_e. On one hand, the asymmetric graphene channel, incorporating the rectangle PPAC array, supports PPRs, which elevates the hot-carrier temperature on the left side of the device. This creates a spatial temperature distribution $T(x)$ across the channel, driving hot carriers from the high-temperature region to the low-temperature region. As a result, the photocurrent I_0 flows along the positive x-axis in all devices, consistent with the p-type doping of graphene under ambient conditions[31]. On the other hand, the electrodes with different work functions (Ti and Cr) induce distinct levels of metal-induced doping in graphene at the two terminals, resulting in a nonuniform local Fermi level $E_f(x)$. This leads to a position-dependent Seebeck coefficient $S(x)$ and built-in potential gradient $\nabla V(x)$, as described by Eqs. (3) and (4). For p-type graphene with a positive $S(x)$, the work function differences ($W_{Gr} > W_{Cr} > W_{Ti}$) cause limited electron transfer from Cr/Au electrode to graphene, but substantial electron transfer from Ti/Au electrode to graphene[32,33]. Consequently, in the Cr/Au–PPAC/graphene–Ti/Au device, the contact-induced current I_e reinforces I_0; in the reversed geometry, I_e partially cancels I_0 (Fig. S17).

The benefit of contact engineering becomes strongest in short channels because the metal-induced doping regions occupy a larger fraction of the total graphene channel. For the Cr/Au–PPAC/graphene–Ti/Au detector, the responsivity increases more rapidly with decreasing L_c than in the symmetric-contact device (Fig. 3h). At L_c = 2 μm, this asymmetric-contact architecture achieves R_V = 1007 V/W, NEP = 16 pW/Hz$^{0.5}$, and D^* = 2.9 × 10^7 Jones when referenced to absorbed power, exceeding the symmetric device by more than one order of magnitude. Work-function engineering therefore amplifies the PTE response driven by resonant THz confinement in the deep-subwavelength channel, while preserving both the linear

photocurrent response to incident power and the frequency-resolved detection capability (Fig. S18).

Finally, we examined how polarization selectivity evolves during channel scaling (Fig. 3i). For L_c = 10 and 20 μm, the devices show inverted figure-eight polar plots that follow the polarization-resolved PPAC absorption, with *PR* values of 32 and 93, respectively. For L_c = 2 μm, the polar plot reverses to a regular figure-eight pattern with *PR* = 9, consistent with the dominant contribution from electrode-mediated field localization in the shortest channel. The scaled detector therefore retains polarization discrimination, while the sign and strength of its polarization response can be controlled by the competition between electrode-induced and PPAC-mediated effects. This tunable competition provides an additional design parameter for monolithic polarimetric THz detectors.

Polarization-resolved THz imaging with deep-subwavelength PPAC detectors

The combined effects of resonant confinement, short-channel transport, and asymmetric contacts place the deep-subwavelength PPAC detector in a distinct performance regime. Unlike most 2D-material-based THz detectors, which rely on external antennas or metamaterial/metasurface couplers, the present device operates without a separate antenna and reaches a minimum channel length of 2 μm, corresponding to ~λ_0/60 at 2.52 THz. A comparison with existing antenna-free 2D THz detectors clearly demonstrates that, despite its compact footprint, the PPAC nano-detector delivers superior performance[5,6,15,16,18,21,22,28,33–45]. When referenced to incident power, the detector achieves R_V = 98 V/W and NEP = 165 pW/Hz$^{0.5}$ (Fig. 4a, b). When referenced to absorbed power, R_V and NEP reach 1007 V/W and 16 pW/Hz$^{0.5}$, respectively. the PPAC nano-detector delivers superior performance. Compared with our previous disk-shaped PPAC detector, the rectangular PPAC design reduces the device area by more than two orders of magnitude while increasing responsivity by over one order of magnitude[5]. Simulations indicate that this improvement originates from stronger field confinement produced by the rectangular PPACs together with the short asymmetric-contact channel (Fig. S19). The key advance is therefore not a single performance metric, but the simultaneous realization of deep-subwavelength footprint, fast PTE response, and intrinsic frequency and polarization selectivity (Supplementary Table S1).

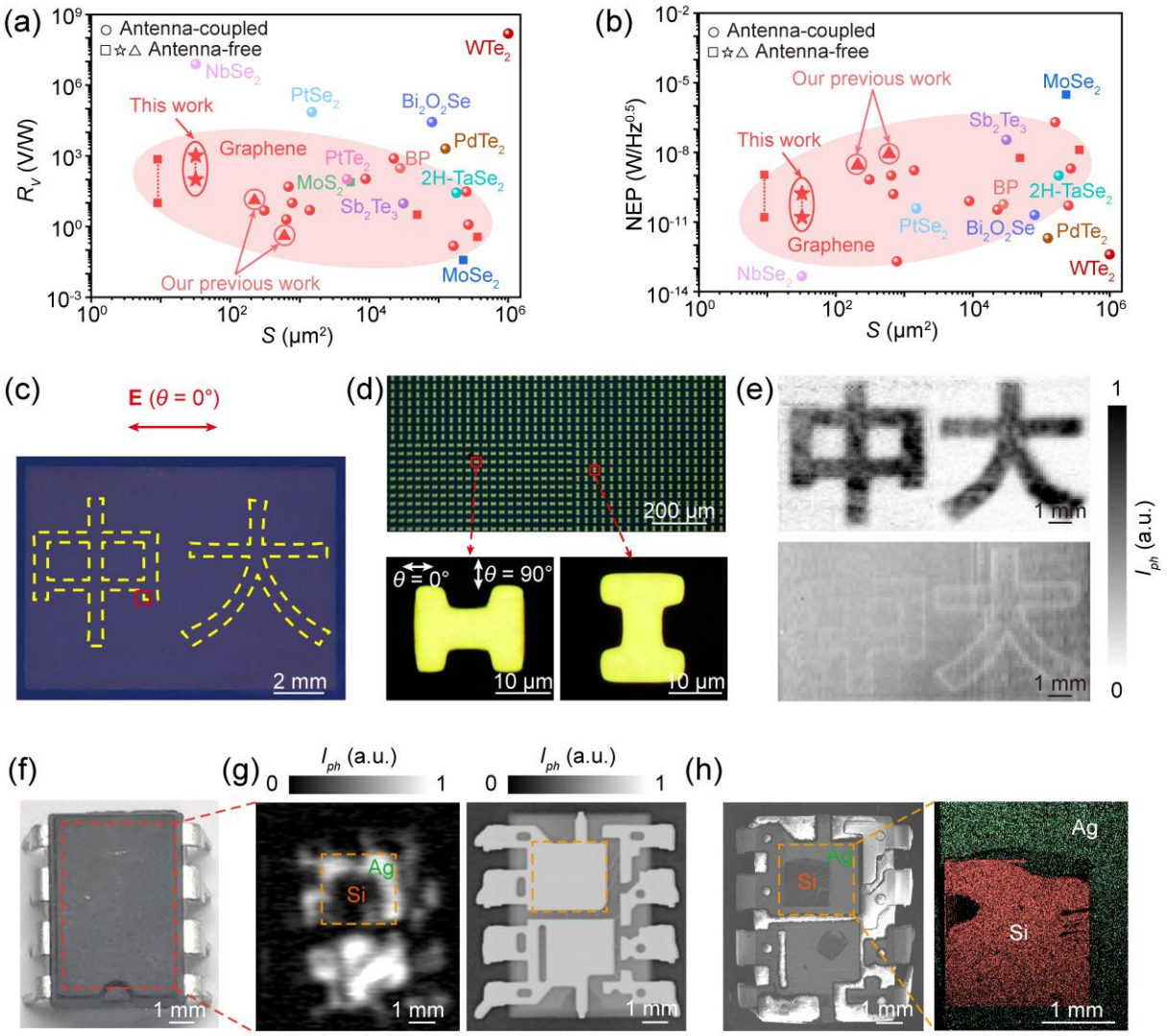

Fig. 4 Polarization-resolved THz imaging and concealed semiconductor-chip inspection. **a**, **b** Comparison of R_V and NEP with room-temperature 2D-material-based THz detectors. **c** Photograph of the imaging target composed of the Chinese characters "中" and "大", where the character regions and surrounding regions contain metal microstructure arrays with orthogonal orientations. **d** Optical images of the H-shaped and inverted-H-shaped metal microstructures. **e** THz images acquired with the PPAC detector (top) and with a commercial polarization-insensitive detector (bottom) at 2.52 THz. **f** Photograph of the power management integrated circuit (PMIC). **g** Polarization-resolved THz image (left) of the capped PMIC acquired with the PPAC detector, compared with a conventional X-ray image (right). The dashed orange region highlights areas with distinct conductivity contrast in the THz image. **h** SEM image (left) and energy-dispersive X-ray spectroscopy (EDS) mapping (right) of the PMIC after cap removal, confirming the material distribution responsible for the THz contrast.

We then used this detector for polarization-resolved THz imaging, where the detected contrast is determined by the polarization state of the transmitted or reflected THz wave rather than by intensity alone. In the transmission experiment, the detector was integrated into a dual-focus scanning imaging system (Fig. S20). A 2.52-THz laser, matched to the detector response peak, illuminated the sample, and a quarter-wave plate converted the incident linear polarization into circular polarization to remove polarization bias from the source. The sample was raster scanned while the detector recorded the transmitted THz signal (see Methods). The imaging target consisted of the Chinese characters "中" and "大" patterned using metallic microstructure arrays with identical dimensions but orthogonal orientations (Fig. 4c, d). The character regions were filled with H-shaped arrays, whereas the surrounding regions were filled with inverted-H-shaped arrays. Simulations show that these microstructure arrays exhibit strong polarization-dependent transmission near 2.52 THz (Fig. S21): the transmittance is nearly zero for $\theta = 0°$ and ~70% for $\theta = 90°$. After circularly polarized THz radiation passes through the object, the character regions and background therefore produce different transmitted polarization states. The PPAC detector selectively converts these polarization differences into photocurrent contrast. The resulting 90 × 50-pixel image, recorded with a 200 μm × 200 μm step size, clearly resolves both characters (Fig. 4e, top). In contrast, a commercial polarization-insensitive Golay cell images only weak outer contours caused by boundary scattering and fails to resolve the internal regions (Fig. 4e, bottom). This comparison demonstrates that the PPAC detector extracts polarization-encoded information that is inaccessible to intensity-only THz detection.

The same polarimetric sensitivity enables concealed material discrimination in semiconductor packages. A capped power management integrated circuit (PMIC, F17D39) contains regions with different carrier concentrations and conductivities, including a silicon chip and an Ag base (Fig. 4f). These regions modify the amplitude and polarization state of the reflected THz field differently[46]. We define the horizontal direction as the long-axis direction of the PPAC unit cell, which is the sensitive axis of the detector (Fig. S22). Fresnel-equation simulations at 2.52 THz show that Ag behaves as a nearly perfect reflector, whereas silicon produces a weaker horizontal field component owing to its lower carrier density and different polarization response. The PPAC detector can therefore map conductivity-related contrast through the cap layer by selectively detecting this horizontal component. Reflective THz imaging was performed with a 2.52-THz beam incident at 45° on the capped PMIC (Fig. S23). The reflected signal was recorded with a 200 μm × 200 μm scan step, giving a spatial resolution of ~400 μm, limited by the ~390 μm diffraction-limited THz spot. The polarization-resolved THz image clearly differentiates the silicon and Ag regions beneath the cap layer (Fig. 4g, left).

After cap removal, optical imaging, SEM, and EDS mapping confirm that the high- and low-contrast regions correspond to the Ag base and silicon chip, respectively (Fig. 4h and Fig. S24). By comparison, conventional X-ray transmission imaging (VJ Technologies, IXS080BP210P396) gives nearly identical grayscale values for these regions and does not reliably distinguish the materials (Fig. 4g, right). The PPAC detector therefore enables a complementary chip-inspection modality based on THz intensity and polarization contrast, providing non-contact access to concealed conductive and semiconducting regions.

Discussion

In summary, we have demonstrated an antenna-free, self-powered THz nano-detector based on rectangular graphene PPACs integrated with asymmetric metal contacts. The rectangular PPAC geometry enables resonance-frequency tuning and polarization discrimination while allowing the graphene channel to be scaled to a deep-subwavelength length of 2 μm, approximately $\lambda_0/60$. Resonant THz confinement preserves light–matter interaction within the atomically thin channel, short-channel scaling accelerates PTE conversion by reducing the hot-carrier diffusion length and electrical parasitics, and work-function-engineered contacts further amplify the built-in thermoelectric response. As a result, the detector achieves broadband operation from 0.53 to 4.24 THz, a polarization ratio of 93, a responsivity of 1007 V/W, an NEP of 16 $pW/Hz^{0.5}$, and a detectivity of 2.9×10^7 Jones, referenced to absorbed THz power. The device exhibits an experimentally measured response time of 230 ps, with simulations indicating a response time down to ~60 ps for the shortest channel. These results show that deep-subwavelength miniaturization, rather than inevitably reducing sensitivity, can provide a route to compact, fast, frequency-, and polarization-resolved room-temperature THz detection. The demonstrated polarization-resolved imaging of concealed semiconductor chips further highlights the potential of PPAC nano-detectors for non-destructive inspection, anisotropic material characterization, and scalable multi-parameter THz focal-plane imaging, particularly when integrated with computational reconstruction or machine-learning algorithms in the future[47].

Materials and methods

Graphene transfer and device fabrication

The high-resistive SiO_2/Si substrate, with a Si thickness of 500 μm, a SiO_2 layer thickness of 300 nm and a resistivity greater than 20000 Ω·cm (Nanjing MKNANO Tech. Co., Ltd. www.mukenano.com), exhibits high transparency and insulation properties in THz region[33]. A

monolayer graphene film (Jiangsu XFNANO Materials Tech. Co., Ltd.), coated with polymethyl methacrylate (PMMA) as a protective mask, was transferred onto the SiO_2/Si substrate via a wet transfer technique. Afterward, the sample was immersed in acetone for one hour to remove the PMMA. The monolayer graphene was patterned using EBL and then etched by oxygen plasma (O_2 at 400 Pa, power of 18 W, etching for 2 min) to create a asymmetric graphene channel with individual rectangle PPAC size of 2.5 μm × 400 nm. Subsequently, the electrodes were defined using ultraviolet maskless lithography machine (TuoTuo Technology, UV Litho-ACA) and coated with Ti/Au or Cr/Au (ZhongNuo Advanced Material (Beijing) Technology Co., Ltd.) in 10 nm/100 nm thicknesses through thermal evaporation. To remove the organic residues, the PPAC nano-detector was annealed in a tube furnace with an Ar/H_2 mixture flow of 150 sccm/350 sccm at 450 °C for 90 min. The device was then affixed to a printed circuit board (PCB) and connected to PCB pads by aluminum wire bonding for further photoresponse characterizations.

Characterizations

The morphology and Raman spectrum of graphene were characterized using a SEM (FEI, Quanta 450) and a confocal Raman spectrometer (Renishaw, Invia Reflex), respectively. The elements of the internal structure of the chip were characterized using an EDS (Oxford Instruments, 51-XMX020). The transmission spectra of graphene rectangle PPACs were tested using a THz time domain spectroscopy (BATOP, TDS-1008). The electrical transport characteristics of the PPAC nano-detector were measured using a source meter (Tektronix, Keithley 2636b). A far-infrared gas laser (Edinburgh Instruments, FIRL 100) with output frequencies of 4.24 THz, 3.11 THz, 2.52 THz, 1.84 THz and 0.53 THz was employed for THz detection. The modulation frequency of the laser was controlled by an optical chopper (SCITEC, 310CD). A low-noise current pre-amplifier (FEMTO, DLPCA-200) was employed to amplify the signals from the PPAC nano-detector, which were subsequently processed using a lock-in amplifier (Stanford, SR830) and a digital phosphor oscilloscope (Tektronix, DPO7354C) for readout. To assess the noise current spectrum of the PPAC nano-detector, a semiconductor parameter analyzer (PDA FS-Pro) was utilized to assess the noise current spectrum of the device.

Photoresponse measurements

In the photoresponse measurement, a laser beam (~ 1 mm spot diameter), modulated by an optical chopper at 225 Hz, was fully irradiated on the device. Fine-tunning was carried out to optimize the photocurrent. The generated photocurrent was then converted to a voltage signal

using a current pre-amplifier and recorded by a lock-in amplifier. For 2D imaging of a specific object, the transmitted light from the imaging object, illuminated by a laser beam modulated at 225 Hz, was directed onto the device to produce photocurrent. The object was scanned using a 2D electrically controlled displacement stage. The photocurrents at each position of the object were measured by a current pre-amplifier and recorded by a lock-in amplifier. By correlating the photocurrent distribution with the scanning positions, a 2D image of the object was reconstructed.

The response time of the PPAC detector was evaluated using THz pulses exhibiting a peak power of 2 mW and a pulse energy of 1.4 μJ. These THz pulses were generated by pumping a $LiNbO_3$ crystal with an 800-nm femtosecond laser (Spectra-Physics, Solstice Ace) and guided by off-axis parabolic mirrors to irradiate onto the PPAC detector. The photovoltage signal generated by the detector, denoted as $R(t)$, underwent amplification via a low-noise preamplifier (FEMTO, DHPCA-100) with a gain of $G = 10^3$ before acquisition by a high-bandwidth oscilloscope (Tektronix DPO7354C, 3.5 GHz bandwidth). The voltage signal $V(t)$ captured by the oscilloscope represents the amplified photovoltage signal, incorporating the temporal delay $M(t)$ introduced by the preamplifier. Consequently, the true photovoltage $R(t)$ was obtained by deconvolving the observed voltage signal $V(t)$ with the delay function $M(t)$ of the preamplifier, expressed as $V(t) = \int_0^t R(t')M(t-t')dt'$. To recover the real photovoltage response of the PPAC detector, a high-speed near-infrared probe was used to calibrate and obtain $\mathrm{F}[M(t)] = \mathrm{F}[V_{\mathrm{IR}}(t)] / \mathrm{F}[R_{\mathrm{IR}}(t)]$, where F denotes the Fourier transform. The actual THz photovoltage response $R_{\mathrm{THz}}(t)$ of the PPAC detector to THz radiation was then determined by deconvolving the observed THz voltage signal $V_{\mathrm{THz}}(t)$ with the delay function $M(t)$ of the preamplifier, defined as $V_{\mathrm{THz}}(t) = \int_0^t R_{\mathrm{THz}}(t')M(t-t')dt'$.

Simulation

The electromagnetic field, temperature field and electric potential distributions of the PPAC nano-detector were calculated using COMSOL. The absorption spectrum of graphene rectangle PPAC array was simulated using FDTD. First, the electromagnetic field distribution was determined using the "Electromagnetic Waves, Frequency Domain (EWFD)" module. The graphene's optical conductivity in the THz region can be defined as,

$$\sigma = \frac{je^2 E_{\mathrm{f}}}{\pi\hbar^2(\omega + j\tau^{-1})} \tag{14}$$

where Fermi level E_f and scattering rate ($\hbar\Gamma = \hbar\tau^{-1}/2$) were set to -0.3 eV and 0.003 eV, respectively. The current density can be expressed as $\boldsymbol{J} = \sigma\boldsymbol{E}$[48]. The refractive indices of the Si and SiO_2 substrates were set to 3.42 and 1.955, respectively[26]. In temperature field distribution simulation, the energy dissipation (heat source) distribution, $q_{absorbed} = 0.5Re(\boldsymbol{J}\cdot\boldsymbol{E}^*)$, calculated from the EWFD module, was input into the "Heat Transfer in Solids (HT)" interface to calculate the temperature distribution, where graphene's thermal conductivity was set to 5300 W/(m·K)[49]. The temperature of graphene PPAC nano-detector can be obtained by,

$$C_p \frac{dT}{dt} = -\nabla \cdot q + Q \tag{15}$$

$$q = -\kappa \nabla T \tag{16}$$

where C_p and κ are the heat capacity and thermal conductivity of graphene, respectivily, and Q is heat source. For the dT/dt term in the equation, it equals zero under steady-state conditions and is non-zero during transient conditions. Since the process of the heat transfer in graphene is primarily mediated by hot carriers, the heat capacity should be set as the carrier heat capacity, which is significantly smaller than the lattice heat capacity (~700 J/(kg·K)). Typically, the heat capacity of hot carriers in graphene is 10^{-2} to 10^{-4} times that of the lattice heat capacity[50], which was set to 10 J/(kg·K).

The "Electric Currents" interface was used to calculate the electric potential V of the PPAC nano-detector, which can be obtained as,

$$\nabla \cdot \boldsymbol{J} = 0 \tag{17}$$

$$\boldsymbol{J} = \sigma_d \boldsymbol{E}_\mathbf{d} \tag{18}$$

$$\boldsymbol{E}_\mathbf{d} = -\nabla V \tag{19}$$

where $\boldsymbol{J}$ is the current density, σ_d and $\boldsymbol{E}_\mathbf{d}$ represent the DC electrical conductivity and DC electric field, respectively. The "Electric Currents" and "Heat Transfer in Solids" interfaces were coupled via the "Thermoelectric Effect" and "Electromagnetic Heating" multiphysics modules, yielding the final temperature and electric potential distributions. Through the thermoelectric coupling module, Eqs. (16) and (18) take the following form as,

$$q = -\kappa \nabla T + P\boldsymbol{J} \tag{20}$$

$$\boldsymbol{J} = \sigma_d \boldsymbol{E}_\mathbf{d} + \boldsymbol{J}_\mathbf{e} \tag{21}$$

Here, $P = ST$ represents the Peltier coefficient, which is the product of the Seebeck coefficient S and temperature T, while $\boldsymbol{J}_\mathbf{e} = -\sigma_d S \nabla T$ represents the hot carrier current density. Based on the Seebeck effect, the electric potential was calculated as Eqs. (3) and (4), where Seebeck coeffficient S were 41.8 μV/K for graphene rectangle PPAC array and 44.3 μV/K for

unpatterned graphene at E_f = -0.3 eV. PPAC nano-detectors with varying channel lengths and two metal electrodes were modeled in COMSOL to calculate the photovoltage. Because the THz beam covers both electrodes, electrode-induced absorption and photocurrent generation were included in the simulations. The THz response, temperature distribution, and electric potential were therefore calculated under the combined contributions of the metal electrodes and the graphene PPAC array. One electrode was grounded, and the potential at the other electrode was taken as the photovoltage, $V_{ph} = V(L_c)$, where L_c is the channel length.

Acknowledgements

The authors acknowledge support from the National Key Basic Research Program of China (grant nos. 2024YFA1208500, 2024YFA1208501, and 2025YFA1213200), the National Natural Science Foundation of China (grant nos. 62605494 and 92463308), Guangdong Basic and Applied Basic Research Foundation (grant no. 2026A1515011655), and China Postdoctoral Science Foundation (grant no. 2025M780806).

Author contributions

H.C., S.D., and N.X. conceived and designed the experiments. Sample fabrication was performed by S.L., X.W., R.L., and H.O.. S.L., Y.K., and R.Z. programmed all equipment. S.L., H.Z., H.C., and S.D. analyzed the results. S.L., and H.Z. performed the experiments and numerical simulations. S.L., H.Z., H.C., and S.D. co-wrote the manuscript with the input of all other coauthors. S.L. and H.Z. contributed equally. All authors have read and agreed to the published version of the manuscript.

Conflict of interest

The authors declare no conflict of interest.

Supplementary Information The online version contains supplementary material available from the author.

Data availability

The data that support the findings of this study are available from the corresponding authors upon reasonable request

References

1. Viti, L., et al. Tracing terahertz plasmon polaritons with a tunable-by-design dispersion in topological insulator metaelements. *Light-Sci. Appl*. **14**, 288 (2025).
2. Ma, J., et al. Security and eavesdropping in terahertz wireless links. *Nature* **563**, 89–93 (2018).
3. Tomasino, A. et al. Large-area photonic circuits for terahertz detection and beam profiling. *Light-Sci. Appl*. **15**, 9 (2026).
4. Soundarapandian, K. P., et al. High-speed graphene-based sub-terahertz receivers enabling wireless communications for 6G and beyond. *Nat. Commun*. **17**, 2627 (2026).
5. Chen, H., et al. Monolithic multiparameter terahertz nano/microdetector based on plasmon polariton atomic cavity. *Adv. Mater*. **37**, 2410946 (2025).
6. Chen, M., Wang, Y. & Zhao, Z. Monolithic metamaterial-integrated graphene terahertz photodetector with wavelength and polarization selectivity. *ACS Nano* **16**, 17263–17273 (2022).
7. Vitiello, M. S. & Viti, L. Engineering THz-frequency light generation, detection, and manipulation through graphene. *Appl. Phys. Rev*. **12**, 011321 (2025).
8. Wang, D., et al. Antiferromagnetic semimetal terahertz photodetectors enhanced through weak localization. *Nat. Commun*. **16**, 25 (2025).
9. Li, X. et al. High-throughput terahertz imaging: progress and challenges. *Light-Sci. Appl*. **12**, 233 (2023).
10. Kravtsov, M., et al. Viscous terahertz photoconductivity of hydrodynamic electrons in graphene. *Nat. Nanotechnol*. **20**, 51–56 (2025).
11. Siday, T., et al. Terahertz detection with perfectly-absorbing photoconductive metasurface. *Nano Lett*. **19**, 2888–2896 (2019).
12 Zhu, Y., et al. On-chip single-crystal plasmonic optoelectronics for efficient hot carrier collection and photovoltage detection. *Light Sci. Appl*. **14**, 325 (2025).
13. Kohli, M., et al. The plasmonic BTO-on-SiN platform–beyond 200 GBd modulation for optical communications. *Light Sci. Appl*. **14**, 399 (2025).
14. Liu, C., et al. Silicon/2D-material photodetectors: from near-infrared to mid-infrared. *Light Sci. Appl*. **10**, 123 (2021).
15. Vicarelli, L., et al. Graphene field-effect transistors as room-temperature terahertz detectors. *Nat. Mater*. **11**, 865–871 (2012).
16. Cai, X., et al. Sensitive room-temperature terahertz detection via the photothermoelectric effect in graphene. *Nat. Nanotechnol*. **9**, 814–819 (2014).

17. Gayduchenko, I., et al. Tunnel field-effect transistors for sensitive terahertz detection. *Nat. Commun*. **12**, 543 (2021).
18. Xu, H., et al. $PtTe_2$-based type-II Dirac semimetal and its van der Waals heterostructure for sensitive room temperature terahertz photodetection. *Small* **15**, 1903362 (2019).
19. Zhang, J., et al. Colossal room-temperature terahertz topological response in type-II Weyl semimetal $NbIrTe_4$. *Adv. Mater*. **34**, 2204621 (2022).
20. Xu, H., et al. Colossal terahertz photoresponse at room temperature: a signature of type-II Dirac fermiology. *ACS Nano* **15**, 5138–5146 (2021).
21. Guo, Q., et al. Efficient electrical detection of mid-infrared graphene plasmons at room temperature. *Nat. Mater.* 17, 986–992 (2018).
22. Guo, C., et al. Anisotropic ultrasensitive $PdTe_2$-based phototransistor for room-temperature long-wavelength detection. *Sci. Adv*. **6**, eabb6500 (2020).
23. Viti, L., et al. M. S. Heterostructured hBN-BP-hBN nano-detectors at THz frequencies. *Adv. Mater*. **28**, 7390 (2016).
24. Duan, S., et al. Linear and phase controllable terahertz frequency conversion via ultrafast breaking the bond of a meta-molecule. *Nat. Commun*. **15**, 1119 (2024).
25. Mao, W., Luan, H. & Ma, R. Singulonics: narwhal-shaped wavefunctions for sub-diffraction-limited nanophotonics and imaging. *eLight* **5**, 27 (2025).
26. Zhu, H., et al. A universal approach for maximizing terahertz wave absorption in graphene cut-wires. *Front. Mater*. **8**, 737347 (2021).
27. Yoshioka, K. et al. Ultrafast intrinsic optical-to-electrical conversion dynamics in a graphene photodetector. *Nat. Photonics* **16**, 718–723 (2022).
28. Viti, L., et al. HBN-encapsulated, graphene-based, room-temperature terahertz receivers, with high speed and low noise. *Nano Lett*. **20**, 3169–3177 (2020).
29. Lu, X. et al. Progress of photodetectors based on the photothermoelectric effect. *Adv. Mater.* **31**, 1902044 (2019).
30. Massicotte, M. et al. Hot carriers in graphene-fundamentals and applications. *Nanoscale* **13**, 8376–8411 (2021).
31. Jahng, J., et al. Characterizing and controlling infrared phonon anomaly of bilayer graphene in optical-electrical force nanoscopy. *Light-Sci. Appl*. **12**, 281 (2023).
32. Gao, L., et al. Broadband, sensitive and spectrally distinctive SnS_2 nanosheet/PbS colloidal quantum dot hybrid photodetector. *Light-Sci. Appl*. **5**, e16126 (2016).
33. Liu, S., et al. A flexible and wearable photodetector enabling ultra-broadband imaging from ultraviolet to millimeter-wave regimes. *Adv. Sci*. **11**, 2401631 (2024).

34. Castilla, S., et al. Fast and sensitive terahertz detection using an antenna-integrated graphene pn junction. *Nano Lett*. **19**, 2765–2773 (2019).

35. Asgari, M., et al. Chip-scalable, room-temperature, zero-bias, graphene-based terahertz detectors with nanosecond response time. *ACS Nano* **15**, 17966–17976 (2021).

36. Auton, G., et al. Terahertz detection and imaging using graphene ballistic rectifiers. *Nano Lett*. **17**, 7015–7020 (2017).

37. Qin, H., et al. Room-temperature, low-impedance and high-sensitivity terahertz direct detector based on bilayer graphene field-effect transistor. *Carbon* **116**, 760–765 (2017).

38. Bandurin, D. A., et al. Resonant terahertz detection using graphene plasmons. *Nat. Commun*. **9**, 5392 (2018).

39. Xie, Y., et al. Defect engineering of MoS_2 for room-temperature terahertz photodetection. *ACS Appl. Mater. Interfaces* **12**, 7351–7357 (2020).

40. Wang, J., et al. Tunable 2H–$TaSe_2$ room-temperature terahertz photodetector. *Chin. Phys. B* **28**, 046802 (2019).

41. Guo, W., et al. Sensitive terahertz detection and imaging driven by the photothermoelectric effect in ultrashort-channel black phosphorus devices. *Adv. Sci*. **7**, 1902699 (2020).

42. Song, Q., et al. Large area flexible thin layer terahertz detector. *Adv. Electron. Mater*. **9**, 2300149 (2023).

43. Chen, Y., et al. Broadband Bi_2O_2Se photodetectors from infrared to terahertz. *Adv. Funct. Mater*. **31**, 2009554 (2021).

44. Li, J., et al. High performance of room-temperature $NbSe_2$ terahertz photoelectric detector. *ACS Appl. Mater. Interfaces* **14**, 14331–14341 (2022).

45. Wang, L., et al. Hybrid Dirac semimetal-based photodetector with efficient low-energy photon harvesting. *Light-Sci. Appl.* **11**, 53 (2022).

46. Nagashima, T. & Hangyo, M. Measurement of complex optical constants of a highly doped Si wafer using terahertz ellipsometry. *Appl. Phys. Lett*. **79**, 3917 (2001).

47. Wu, N., et al. Intelligent nanophotonics: when machine learning sheds light. *eLight* **5**, 5 (2025).

48. Falkovsky, L. A. Optical properties of graphene. *J. Phys. Conf. Ser*. **129**, 012004 (2008).

49. Safaei, A., et al. Dirac plasmon-assisted asymmetric hot carrier generation for room-temperature infrared detection. *Nat. Commun*. **10**, 3498 (2019).

50. Song, J. C. W., et al. Hot carrier transport and photocurrent response in graphene. *Nano Lett*. **11**, 4688–4692 (2011).

Supplementary Files

This is a list of supplementary files associated with this preprint. Click to download.

- shortchanelgrapheneatomiccavityTHzdetectorLSASIv4.docx